
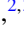








Anisotropic signatures of electronic correlations in the electrical resistivity of UTe_2

T. Thebault ¹, M. Vališka ^{2,3}, G. Lapertot ², A. Pourret ², D. Aoki ⁴, G. Knebel ², D. Braithwaite ² and W. Knafo ¹

¹Laboratoire National des Champs Magnétiques Intenses - EMFL, CNRS, Université Grenoble Alpes,

INSA-T, Université Toulouse 3, 31400 Toulouse, France

²Université Grenoble Alpes, CEA, Grenoble INP, IRIG, PHELIQS, 38000 Grenoble, France

³Charles University, Faculty of Mathematics and Physics, Department of Condensed Matter Physics,
Ke Karlovu 5, Prague 2, 121 16, Czech Republic

⁴Institute for Materials Research, Tohoku University, Ikaraki 311-1313, Japan



(Received 31 May 2022; revised 15 September 2022; accepted 16 September 2022; published 7 October 2022)

Multiple unconventional superconducting phases are suspected to be driven by magnetic fluctuations in the heavy-fermion paramagnet UTe_2 , and a challenge is to identify the signatures of the electronic correlations, including the magnetic fluctuations, in the bulk physical quantities. Here, we investigate thoroughly the anisotropy of the electrical resistivity of UTe_2 under intense magnetic fields up to 70 T, for different electrical-current and magnetic-field configurations. Two characteristic temperatures and an anisotropic low-temperature Fermi-liquid-like coefficient A , controlled by the electronic correlations, are extracted. Their critical behavior near the metamagnetic transition induced at $\mu_0 H_m \simeq 35$ T for $\mathbf{H} \parallel \mathbf{b}$ is characterized. Anisotropic scattering processes are evidenced and magnetic fluctuations are proposed to contribute, via a Kondo hybridization, to the electrical resistivity. Our work appeals for a microscopic modeling of the anisotropic contributions to the electrical resistivity as a milestone for understanding magnetically mediated superconductivity in UTe_2 .

DOI: [10.1103/PhysRevB.106.144406](https://doi.org/10.1103/PhysRevB.106.144406)

I. INTRODUCTION

Magnetic fluctuations are suspected to be at the origin of the superconducting pairing mechanism in many unconventional superconductors [1]. However, a difficulty is to reveal experimentally the intimate relationship between the magnetic and superconducting properties. The recent discovery of unconventional superconductivity in the paramagnetic compound UTe_2 [2,3,4] opened a new route to investigate the interplay between magnetism and unconventional superconductivity. A spin-triplet nature of superconducting pairing has been proposed for this compound initially presented as a nearly ferromagnetic system. Spin-triplet superconductivity in UTe_2 is supported by the observation of a critical superconducting field exceeding the Pauli limitation expected for the three crystallographic directions [2,5] and by nuclear-magnetic-resonance (NMR) Knight-shift experiments made in the superconducting (SC) state [2,6,7]. Superconductivity is reinforced near a first-order metamagnetic transition induced at a magnetic field $\mu_0 H_m = 35$ T applied along the hard direction \mathbf{b} [2,5,8,9,10]. A phase transition between the low-field superconducting phase SC1 and a high-field superconducting phase SC2 was identified by heat capacity at ambient pressure [11] and by tunnel-diode-oscillator technique under pressure [12]. The phase SC2 suddenly collapses in fields higher than H_m [5,10,13], where an abrupt Fermi-surface change was also reported [14]. The metamagnetic transition turns into a crossover at temperatures higher than $T_{CEP} \simeq 5 - 7$ K, which corresponds to a critical endpoint [8,13]. The crossover vanishes near the temperature $T_{\chi_b}^{\max} = 35$ K, where the magnetic susceptibility measured for

$\mathbf{H} \parallel \mathbf{b}$ shows a broad maximum at low fields [2,8,9,15]. As in many heavy-fermion paramagnets, H_m and $T_{\chi_b}^{\max}$ delimitate a correlated paramagnetic (CPM) regime and a polarized paramagnetic (PPM) regime is established for $H > H_m$ [16,17]. Field-induced reinforcement of superconductivity rapidly disappears when the magnetic field is tilted away from \mathbf{b} , and a second field-induced superconducting phase, labeled SC-PPM, develops in the PPM regime close to $\mu_0 H_m \simeq 45$ T in a magnetic field tilted by 30° from \mathbf{b} to \mathbf{c} [5,10,13]. Multiple superconducting and magnetic phases have also been evidenced under pressure, leading to complex three-dimensional pressure - magnetic field - temperature phase diagrams illustrating the subtle interplay between magnetism and superconductivity in UTe_2 [12,18–26].

Contrary to early expectations [2], inelastic-neutron-scattering experiments showed the presence of low-dimensional antiferromagnetic fluctuations, but no indication for ferromagnetic fluctuations so far [27–29]. These antiferromagnetic fluctuations, peaked at the incommensurate wave vector $\mathbf{k}_1 = (0, 0.57, 0)$, saturate below the characteristic temperature $T_1^* = 15$ K [28] and become gapped in the superconducting phase [30,31]. They may, therefore, play a role for the superconducting pairing mechanism. Electrical-resistivity measurements further revealed a broad maximum at the temperature $T_{\rho_{zz}}^{\max} \simeq 15$ K for a current $\mathbf{I} \parallel \mathbf{c}$ and the possible role of magnetic fluctuations was emphasized [32]. Higher temperature scales $T_{\rho_{xx}}^{\max} \simeq T_{\rho_{yy}}^{\max} \simeq 60 - 70$ K were also revealed at broad maxima of the electrical resistivity measured with \mathbf{I} applied along \mathbf{a} and \mathbf{b} , respectively [32]. The anisotropy of the electrical resistivity presumably results from the combination

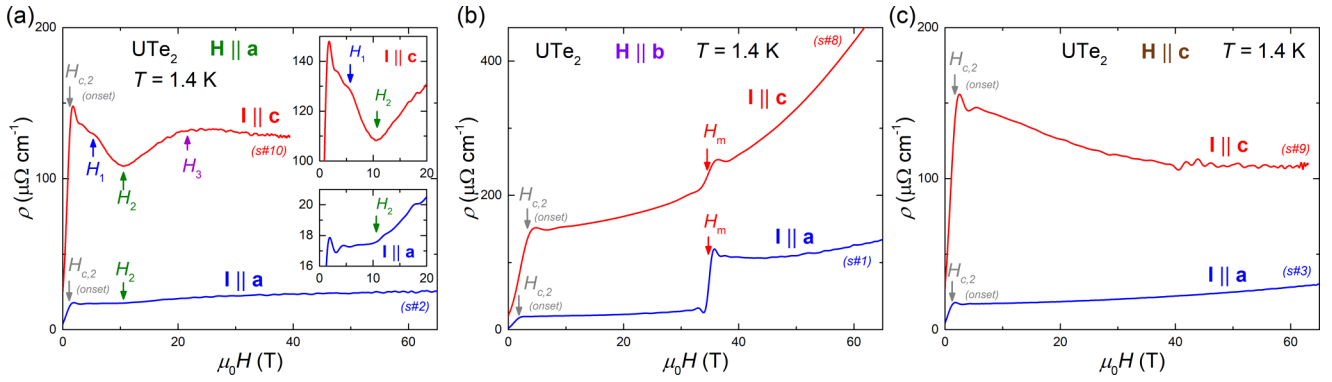


FIG. 1. Magnetic-field dependence of the electrical resistivities ρ_{xx} and ρ_{zz} , measured with currents $\mathbf{I} \parallel \mathbf{a}$ and $\mathbf{I} \parallel \mathbf{c}$, respectively, of UTe_2 at the temperature $T = 1.4 \text{ K}$ under magnetic fields (a) $\mathbf{H} \parallel \mathbf{a}$, (b) $\mathbf{H} \parallel \mathbf{b}$, (c) $\mathbf{H} \parallel \mathbf{c}$. Zooms to low-fields $\mu_0 H < 20 \text{ T}$ are shown in the insets of (a).

of anisotropic magnetic and Fermi-surface properties. Anisotropic magnetic fluctuations from moments along the easy magnetic axis \mathbf{a} were evidenced by NMR relaxation-rate measurements [33], and cylindrical Fermi surfaces along the direction \mathbf{c} expected from electronic-structure calculations have been confirmed by angle-resolved-photoemission spectroscopy [34–36]. A challenge is now to determine how the magnetic fluctuations and the band structure are modified in a magnetic field, in particular when field-induced superconductivity is stabilized.

In this work, we focus on a systematic investigation of the electrical resistivity of UTe_2 under high magnetic fields $\mu_0 \mathbf{H}$ up to 70 T applied along the three crystallographic directions \mathbf{a} , \mathbf{b} , and \mathbf{c} . We compare new sets of data corresponding to the configuration $\mathbf{I} \parallel \mathbf{c}$ to data with the configuration $\mathbf{I} \parallel \mathbf{a}$, published initially in Ref. [8] and reanalyzed here. The evolution of the resistivity maxima observed for $\mathbf{I} \parallel \mathbf{a}$, \mathbf{c} are characterized. Two temperatures characterizing the electronic correlations are identified and their magnetic-field evolutions are determined, allowing us to construct magnetic-field-temperature phase diagrams for the three directions of magnetic field. At low temperatures, Fermi-liquid-like fits to the resistivity data let us extracting the quadratic coefficient A , whose anisotropic behavior in high magnetic field is evidenced. The possible roles played by magnetic fluctuations and Kondo hybridization are discussed.

II. METHODS

Single crystals were grown by chemical vapor transport [2,3]. Their orientation was checked at room temperature using a Laue diffractometer. Oriented plates were prepared using an electrical-spark cutter. After cutting, a surface was polished and 15- μm gold wires were spot-welded along the larger dimension of the surface. Samples measured with an electrical current $\mathbf{I} \parallel \mathbf{c}$ had dimensions of approximately 1–2 mm along \mathbf{c} , 0.3–0.5 mm along \mathbf{a} and 0.1–0.3 mm along \mathbf{b} . Samples measured with an electrical current $\mathbf{I} \parallel \mathbf{a}$ had dimensions of approximately 1–2 mm along \mathbf{a} , 0.5 mm along \mathbf{b} and 0.1–0.3 mm along \mathbf{c} . Electrical-resistivity measurements have been performed using 70-T pulsed-field magnets at the Laboratoire National des Champs Magnétiques Intenses in

Toulouse. A 6-MJ generator was used to generate pulses of 30-ms-rise and 150-ms-fall durations. Temperature and magnetic-field variations of the resistivity are presented for the up-sweep and the variations of the quadratic coefficient A are presented for both up- and down-sweeps (more data from up- and down-sweeps are shown in the Appendix). Pulsed-field experiments were performed at constant temperatures from 1.4 to 80 K using a ^4He cryostat. Resistivity was measured by the four-point technique, with electrical currents at frequencies between 20 and 40 kHz and a digital lock-in analysis. For each current direction, measurements under magnetic field directions $\mathbf{H} \parallel \mathbf{a}$, \mathbf{b} , and \mathbf{c} were made on three samples simultaneously (samples #1, #2, and #3 with $\mathbf{I} \parallel \mathbf{a}$ and samples #8, #9, and #10 with $\mathbf{I} \parallel \mathbf{c}$). The resistivity data were normalized to absolute values following measurements made at the CEA-Grenoble on samples with well-defined geometrical shapes [37]. The ρ_{xx} resistivity data of samples with $\mathbf{I} \parallel \mathbf{a}$, initially published in Ref. [8], have been reanalyzed using a geometric factor consistent with data published in [13]. This reanalysis led to different absolute values of the extracted Fermi-liquid coefficient A . A background subtraction, not performed in the original paper, was also done on ρ_{xx} versus temperature T data, as well as it was done on the new ρ_{xx} data measured with a current $\mathbf{I} \parallel \mathbf{c}$. Our absolute values of the electrical resistivity with $\mathbf{I} \parallel \mathbf{a}$ and $\mathbf{I} \parallel \mathbf{c}$ are 20–30% larger than those determined by Eo *et al.* [32]. In spite of these differences, similar anisotropy of the electrical resistivity is extracted for both sets of data.

III. RESULTS

A. Low-temperature electrical resistivity

Figure 1 compares the electrical resistivity versus magnetic field of UTe_2 at $T = 1.4 \text{ K}$ for $\mathbf{I} \parallel \mathbf{a}$ and \mathbf{c} , for the three magnetic field directions $\mathbf{H} \parallel \mathbf{a}$, \mathbf{b} , and \mathbf{c} . The temperature $T = 1.4 \text{ K}$ is slightly below the superconducting temperature $T_{sc} \simeq 1.6 - 1.7 \text{ K}$ and all curves show the superconducting-to-normal-state transition at an upper critical field $\mu_0 H_{c2}$ of a few T, defined here at the kink preceding the restoration of the normal state. Figure 1(a) shows that, in a magnetic field $\mathbf{H} \parallel \mathbf{a}$, three anomalies characterize broad crossovers for $\mathbf{I} \parallel \mathbf{c}$ at the magnetic fields $\mu_0 H_1 \simeq 6 \text{ T}$, $\mu_0 H_2 \simeq 10 \text{ T}$ and

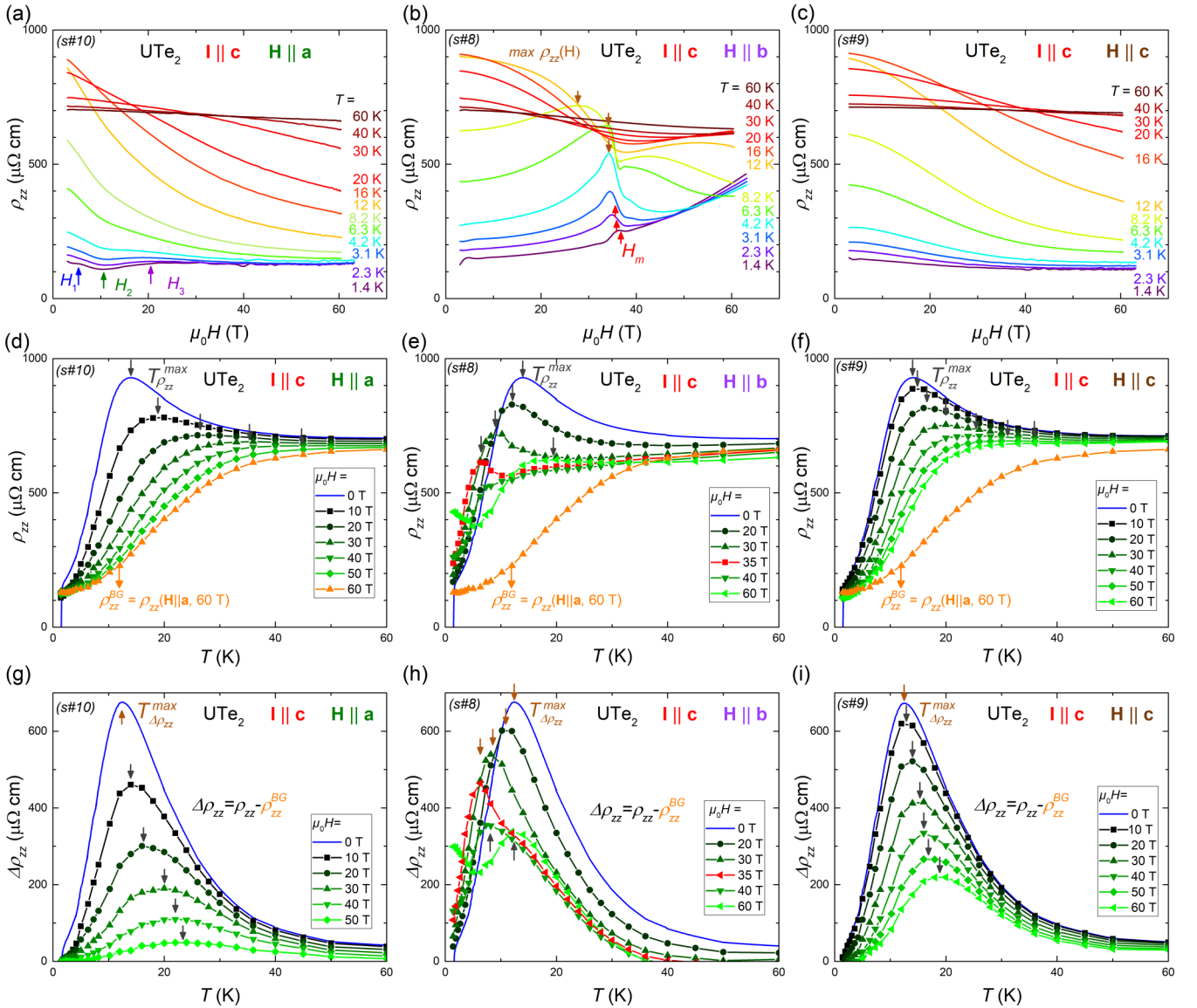


FIG. 2. Magnetic-field dependence of the electrical resistivity ρ_{zz} , measured with $\mathbf{I} \parallel \mathbf{c}$, of UTe₂ at temperatures from 1.4 to 60 K under magnetic fields (a) $\mathbf{H} \parallel \mathbf{a}$, (b) $\mathbf{H} \parallel \mathbf{b}$, and (c) $\mathbf{H} \parallel \mathbf{c}$. Temperature dependence of ρ_{zz} at constant magnetic fields (d) $\mu_0 \mathbf{H} \parallel \mathbf{a}$, (e) $\mu_0 \mathbf{H} \parallel \mathbf{b}$, and (f) $\mu_0 \mathbf{H} \parallel \mathbf{c}$ up to 60 T. Temperature dependence of $\Delta\rho_{zz}$, extracted after subtraction of a background estimated as $\rho_{zz}(\mathbf{H} \parallel \mathbf{a}, 60 \text{ T})$, at constant magnetic fields (g) $\mu_0 \mathbf{H} \parallel \mathbf{a}$, (h) $\mu_0 \mathbf{H} \parallel \mathbf{b}$, and (i) $\mu_0 \mathbf{H} \parallel \mathbf{c}$ up to 60 T.

$\mu_0 H_3 \simeq 20 \text{ T}$, in agreement with a previous report [38], while only a broad kink is observed at H_2 for $\mathbf{I} \parallel \mathbf{a}$. Figure 1(b) shows that, in a magnetic field $\mathbf{H} \parallel \mathbf{b}$, the first-order metamagnetic transition at $\mu_0 H_m = 35 \text{ T}$ induces a much larger jump for $\mathbf{I} \parallel \mathbf{a}$ than for $\mathbf{I} \parallel \mathbf{c}$. Figure 1(c) shows that, for $\mathbf{H} \parallel \mathbf{c}$, beyond the superconducting transition, no anomaly is induced by a magnetic field for both current directions, and ρ_{xx} monotonously increases with H while ρ_{zz} monotonously decreases with H . A H^2 increase of the resistivity found for two transverse configurations ($\mathbf{I} \parallel \mathbf{c}, \mathbf{H} \parallel \mathbf{b}$) and ($\mathbf{I} \parallel \mathbf{a}, \mathbf{H} \parallel \mathbf{c}$) is ascribed to field-induced contributions from charge carriers [see Figs. 1(b) and 1(c) and the Appendix]. In the following, we present a detailed study of the temperature dependence of electrical-resistivity-versus-magnetic-field data of UTe₂ measured within the six configurations considered here.

B. Electrical resistivity with $\mathbf{I} \parallel \mathbf{c}$

Figure 2 presents electrical-resistivity data of UTe₂ measured with a current $\mathbf{I} \parallel \mathbf{c}$, either as function of magnetic field for different temperatures from 1.4 to 60 K [(a)–(c)], or as function of temperature for different magnetic fields up to 60 T [(d)–(i)], for the three configurations with $\mathbf{H} \parallel \mathbf{a}$, \mathbf{b} , and \mathbf{c} .

For $\mathbf{H} \parallel \mathbf{a}$ [Fig. 2(a)], the anomalies at the fields H_1 , H_2 and H_3 show signatures at temperatures up to $T \approx 5 \text{ K}$ (see the Appendix). At temperatures $T > 5 \text{ K}$, ρ_{zz} monotonously decreases with H . For $\mathbf{H} \parallel \mathbf{b}$ [Fig. 2(b)], the low-temperature steplike increase of ρ_{zz} observed at the metamagnetic field H_m changes into a decrease at higher temperatures. The resistivity jump is accompanied by a hysteresis emphasized in field-derivative $\partial\rho_{zz}/\partial H$ plots (shown for up- and down-sweeps in

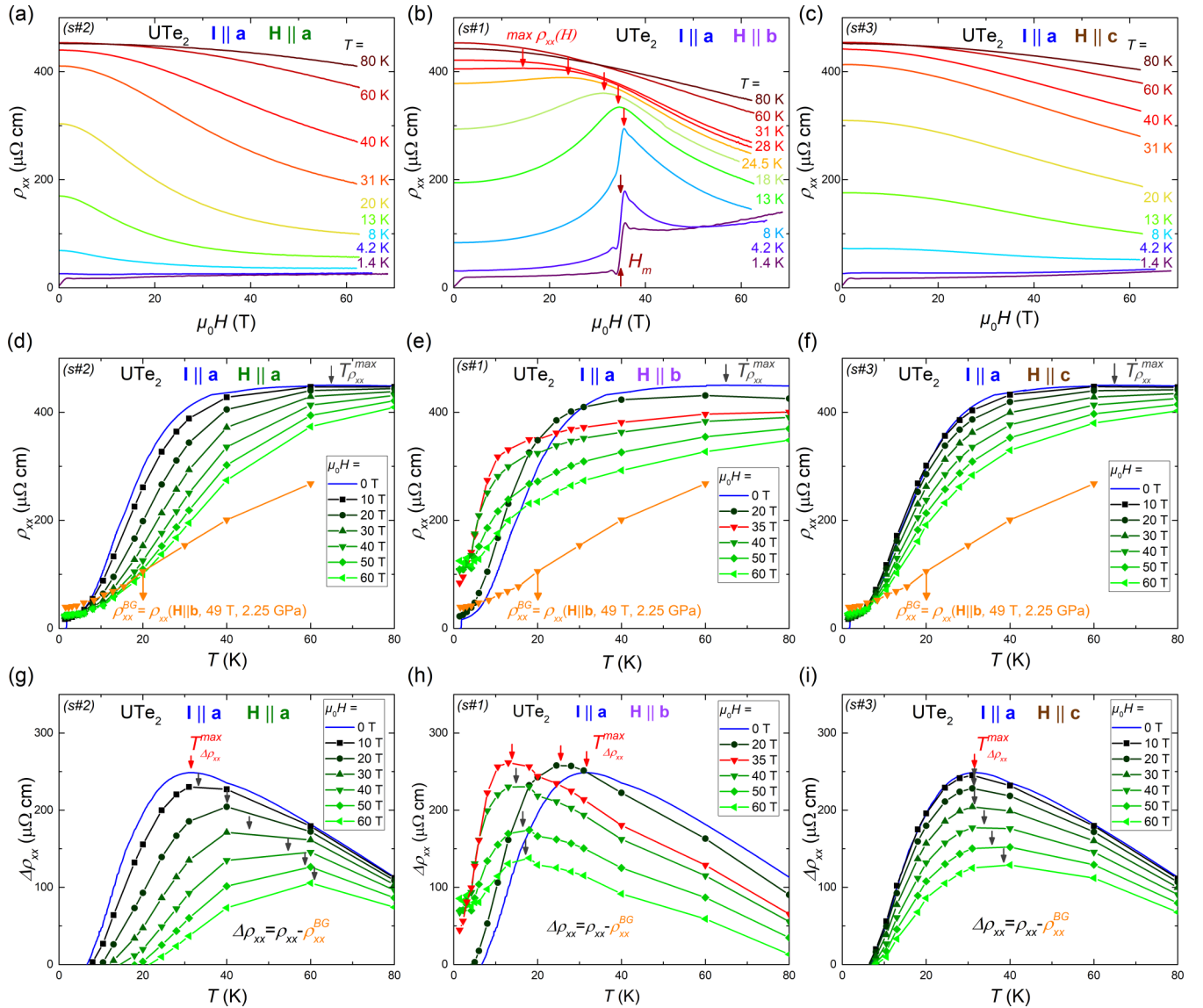


FIG. 3. Magnetic-field dependence of the electrical resistivity ρ_{xx} , measured with $\mathbf{I} \parallel \mathbf{a}$, of UTe_2 at temperatures from 1.4 to 60 K under magnetic fields (a) $\mathbf{H} \parallel \mathbf{a}$, (b) $\mathbf{H} \parallel \mathbf{b}$, and (c) $\mathbf{H} \parallel \mathbf{c}$. Temperature dependence of ρ_{xx} at constant magnetic fields (d) $\mu_0\mathbf{H} \parallel \mathbf{a}$, (e) $\mu_0\mathbf{H} \parallel \mathbf{b}$, and (f) $\mu_0\mathbf{H} \parallel \mathbf{c}$ up to 60 T. Temperature dependence of $\Delta\rho_{xx}$, extracted after subtraction of a background estimated as $\rho_{xx}(\mathbf{H} \parallel \mathbf{b}, 49 \text{ T}, 2.25 \text{ GPa})$, at constant magnetic fields (g) $\mu_0\mathbf{H} \parallel \mathbf{a}$, (h) $\mu_0\mathbf{H} \parallel \mathbf{b}$, and (i) $\mu_0\mathbf{H} \parallel \mathbf{c}$ up to 60 T.

the Appendix). We lose the trace of the hysteresis at a temperature of 6 K, where the critical endpoint can be defined, and beyond which the metamagnetic first-order transition at H_m characterized by a step variation in ρ_{zz} turns into a crossover characterized by a broad maximum in $\rho_{zz}(H)$. The crossover field decreases with increasing temperature and disappears for $T \geq 12 \text{ K}$. In this transversal configuration, an increase of ρ_{zz} is observed at low temperature for $\mu_0H \geq 40 \text{ T}$. In this regime, ρ_{zz} follows a H^2 behavior, which is presumably controlled by a field-induced cyclotron motion of carriers (see Appendix). For $\mathbf{H} \parallel \mathbf{c}$ [Fig. 2(c)], no anomalies are detected and the resistivity monotonously decreases at all temperatures.

Figures 2(d)–2(f) show resistivity ρ_{zz} versus T data at constant magnetic field. These data were extracted from ρ_{zz} versus H data measured at constant temperature [see Figs. 2(a)–2(c)]. For $\mathbf{H} \parallel \mathbf{a}$ [Fig. 2(d)] and $\mathbf{H} \parallel \mathbf{c}$ [Fig. 2(f)], the maximum

of ρ_{zz} is shifted to higher temperature from $T_{\rho_{zz}}^{\max} \approx 14 \text{ K}$ at $H = 0$ to $T_{\rho_{zz}}^{\max} > 40 \text{ K}$ at $\mu_0H \gtrsim 50 \text{ T}$. The maximal value of $\rho_{zz}(T)$ decreases when the magnetic field increases and the decrease is faster for $\mathbf{H} \parallel \mathbf{a}$ than for $\mathbf{H} \parallel \mathbf{c}$. For $\mathbf{H} \parallel \mathbf{b}$ [Fig. 2(e)], the temperature $T_{\rho_{zz}}^{\max}$ decreases for $H < H_m$, it cannot be defined at fields slightly higher than H_m , and it increases for $H > H_m$. The low-temperature increase of ρ_{xx} at high fields, presumably controlled by the cyclotron motion of carriers, is emphasized in Fig. 2(e).

For the three directions of magnetic field, a maximum in ρ_{zz} versus T cannot be defined in fields above 30–40 T. Here, we propose to subtract from ρ_{zz} a background term ρ_{zz}^{BG} , estimated as $\rho_{zz}(\mathbf{H} \parallel \mathbf{a}, 60 \text{ T})$ measured in a magnetic field $\mu_0\mathbf{H} \parallel \mathbf{a}$ of 60 T. This background is characteristic of the high-field PPM regime. In a magnetic field $\mu_0\mathbf{H} \parallel \mathbf{a}$ of 60 T, a saturation of the low-temperature magnetization [39] indicates that most of the magnetic fluctuations have been quenched,

which possibly drives the loss of the low-temperature contribution to the electrical resistivity observed here (see the Appendix and Ref. [40]). Figures 2(g)–2(i) show the temperature dependence of $\Delta\rho_{zz}$, for $\mathbf{H} \parallel \mathbf{a}$, \mathbf{b} , and \mathbf{c} , respectively, estimated after subtraction of the resistivity background ρ_{zz}^{BG} . The temperature $T_{\Delta\rho_{zz}}^{\max}$ ($= 12.5$ K at $H = 0$) defined at the maximum of $\Delta\rho_{zz}$ versus T is slightly smaller than $T_{\rho_{zz}}^{\max}$ ($= 14$ K at $H = 0$) defined at the maximum of ρ_{zz} versus T . For $\mathbf{H} \parallel \mathbf{a}$ [Fig. 2(g)], the fast decrease of $\Delta\rho_{zz}$ with increasing $\mu_0 H$ up to 50 T is accompanied by an increase of $T_{\Delta\rho_{zz}}^{\max}$ by almost a factor two. For $\mathbf{H} \parallel \mathbf{c}$ [Fig. 2(i)], a slower decrease of $\Delta\rho_{zz}$ is accompanied by a slower increase of $T_{\Delta\rho_{zz}}^{\max}$. For $\mathbf{H} \parallel \mathbf{b}$ [Fig. 2(h)], both the CPM regime for $H < H_m$ and the PPM regime for $H > H_m$ are characterized by a maximum of $\Delta\rho_{zz}$ versus T , and the metamagnetic transition at H_m is accompanied by a minimal value of $T_{\Delta\rho_{zz}}^{\max}$.

C. Electrical resistivity with $\mathbf{I} \parallel \mathbf{a}$

Figure 3 presents electrical-resistivity data of UTe_2 measured with a current $\mathbf{I} \parallel \mathbf{a}$, either as function of magnetic field for different temperatures from 1.4 to 80 K [(a)–(c)], or as function of temperature for different magnetic fields up to 60 T [(d)–(i)], for the three configurations with $\mathbf{H} \parallel \mathbf{a}$, \mathbf{b} , and \mathbf{c} (data initially published in [8] and reanalyzed here).

Figures 3(a)–3(c) show ρ_{xx} versus H measured at constant temperatures with a magnetic field along \mathbf{a} , \mathbf{b} , and \mathbf{c} , respectively. For $\mathbf{H} \parallel \mathbf{a}$ [Fig. 3(a)], a kink is observed at H_2 for temperatures $T \lesssim 4$ K (a zoom is provided in the Appendix). For $\mathbf{H} \parallel \mathbf{b}$ [Fig. 3(b)], the steplike increase of ρ_{xx} at H_m turns into a broad maximum at temperatures above $T_{CEP} \simeq 7$ K. This maximum shifts to lower magnetic fields when the temperature is further increased above T_{CEP} , before vanishing at temperatures $T > 30$ K. The hysteresis of the first-order metamagnetic transition is characterized through $\partial\rho_{xx}/\partial H$ versus H plots for up- and down-sweeps (see the Appendix). Finally, for $\mathbf{H} \parallel \mathbf{c}$ [Fig. 3(c)], the ρ_{xx} versus H curves monotonously increase for $T < 5$ K and they monotonously decrease for $T > 5$ K. For this transversal configuration, ρ_{xx} follows a H^2 behavior at low temperature, which may possibly be controlled by a field-induced cyclotron motion of carriers (see the Appendix). The low-temperature enhancement of ρ_{xx} visible in fields $\mu_0\mathbf{H} \parallel \mathbf{b}$ higher than 40 T [Fig. 3(b)] may also be controlled by cyclotron motion of carriers.

Figures 3(d)–3(f) show the resistivity ρ_{xx} versus T at constant magnetic fields extracted from field-scans of ρ_{xx} at constant temperatures [see Figs. 3(a)–3(c)]. The temperature $T_{\rho_{xx}}^{\max}$ at the maximum of ρ_{xx} equals ~ 65 K at zero field and increases with increasing magnetic fields $\mathbf{H} \parallel \mathbf{a}$ and $\mathbf{H} \parallel \mathbf{c}$. For $\mathbf{H} \parallel \mathbf{b}$, $T_{\rho_{xx}}^{\max}$ decreases with H for $H < H_m$ and increases with H for $H > H_m$.

The maximum in ρ_{xx} versus T is not well-defined in high magnetic fields as the anomaly becomes broader and less intense. To characterize this crossover, we propose to subtract from ρ_{xx} a background term ρ_{xx}^{BG} , estimated as the resistivity $\rho_{xx}(\mathbf{H} \parallel \mathbf{b}, 49 \text{ T}, 2.25 \text{ GPa})$ measured in a magnetic field $\mu_0\mathbf{H} \parallel \mathbf{b}$ of 49 T combined with a pressure of 2.25 GPa and published in [26]. This background is representative from a state deep inside the PPM regime [23], where most of the magnetic fluctuations and electronic correlations have been

quenched (see the Appendix). Figures 3(g)–3(i) show $\Delta\rho_{xx}$ versus T data for magnetic fields along \mathbf{a} , \mathbf{b} , and \mathbf{c} , respectively, extracted after subtraction of the estimated background ρ_{xx}^{BG} . The temperature $T_{\Delta\rho_{xx}}^{\max}$ defined at the maximum of $\Delta\rho_{xx}$ versus T is much smaller than $T_{\rho_{xx}}^{\max}$ defined at the maximum of ρ_{xx} versus T ($T_{\Delta\rho_{xx}}^{\max} \simeq 32 \text{ K} < T_{\rho_{xx}}^{\max} \simeq 65 \text{ K}$ at $H = 0$) [40]. Under magnetic fields, $T_{\Delta\rho_{xx}}^{\max}$ varies in a similar manner than $T_{\Delta\rho_{zz}}^{\max}$ extracted in Sec. III B: it monotonously increases with H for $\mathbf{H} \parallel \mathbf{a}$ [Fig. 3(g)] and $\mathbf{H} \parallel \mathbf{c}$ [Fig. 3(i)], the increase being faster for $\mathbf{H} \parallel \mathbf{a}$, and it passes through a minimal value at the metamagnetic field H_m for $\mathbf{H} \parallel \mathbf{b}$ [Fig. 3(h)]. For the three field directions, the amplitude of the anomaly in $\Delta\rho_{xx}$ is strongly reduced in high magnetic fields, being compatible with a field-induced loss of the electronic correlations.

D. Phase diagrams and quantum critical properties

Figure 4 presents the magnetic-field-temperature phase diagrams of UTe_2 for $\mathbf{H} \parallel \mathbf{a}$, \mathbf{b} , and \mathbf{c} , constructed using data from this work and data from Refs. [10,13]. The zero-field values of $T_{\Delta\rho_{xx}}^{\max} \simeq 32$ K and $T_{\Delta\rho_{zz}}^{\max} \simeq 12.5$ K coincide with the temperatures $T_{\chi_b}^{\max} \simeq 35$ K and $T_{\chi_a}^{\text{kink}} \simeq 15$ K, where anomalies are observed in the low-field magnetic susceptibilities χ_b and χ_a , respectively [4,13,15,23]. For the three magnetic-field directions, the two temperatures $T_{\Delta\rho_{xx}}^{\max}$ and $T_{\Delta\rho_{zz}}^{\max}$ further have similar field dependences, indicating related associated phenomena. Under a magnetic field \mathbf{H} applied along the easy magnetic axis \mathbf{a} [Fig. 4(a)], the fast polarization of the magnetic moments is accompanied by three successive anomalies in the low-temperature electrical resistivity, at $\mu_0 H_1 \simeq 6$ T, $\mu_0 H_2 \simeq 10$ T and $\mu_0 H_3 \simeq 20$ T. H_1 coincides with a maximum in the field derivative of the magnetization [9] and a minimum in the thermoelectric power, which was identified as a signature of a Lifshitz transition [38]. The polarization of the magnetic moments is accompanied by a monotonous increase with H of the two temperature scales $T_{\Delta\rho_{xx}}^{\max}$ and $T_{\Delta\rho_{zz}}^{\max}$ characterizing the electronic correlations. Under magnetic field \mathbf{H} applied along the hard magnetic axis \mathbf{c} [Fig. 4(c)], a slower magnetic polarization [39] is accompanied by a larger upper critical field $\mu_0 H_{c2} \simeq 10$ T of the low-temperature superconducting phase, but there are no additional field-induced anomalies in resistivity or magnetization data. A monotonous increase with H of $T_{\Delta\rho_{xx}}^{\max}$ and $T_{\Delta\rho_{zz}}^{\max}$ is also observed. For $\mathbf{H} \parallel \mathbf{b}$, which is the hardest magnetic axis [Fig. 4(b)], $T_{\Delta\rho_{xx}}^{\max}$ and $T_{\Delta\rho_{zz}}^{\max}$ both decrease with H and merge near to the critical end point at the temperature $T_{CEP} \simeq 7$ K, below which a first-order transition at the metamagnetic field $\mu_0 H_m \simeq 35$ T marks the onset of the PPM regime. For $H < H_m$, $T_{\Delta\rho_{xx}}^{\max}$ and $T_{\Delta\rho_{zz}}^{\max}$ are characteristic temperature scales of the CPM regime. For $H > H_m$, $T_{\Delta\rho_{xx}}^{\max}$ and $T_{\Delta\rho_{zz}}^{\max}$ increase and can then be considered as characteristic temperature scales of the PPM regime. While the low-temperature superconducting phase SC1 is delimited by an upper critical field $\mu_0 H_{c2} \simeq 15$ T [11], the field-induced superconducting phase SC2, stabilized near H_m , vanishes at fields higher than H_m , in the PPM regime.

Within a Fermi-liquid behavior, the electrical resistivity follows a quadratic temperature dependence $\rho(T) = \rho_0 + AT^2$, where A is related to the effective mass m^* by $A \propto m^{*2}$. In heavy-fermion compounds, the effective mass m^* is large, typically of the order of hundred times the free-electron mass,

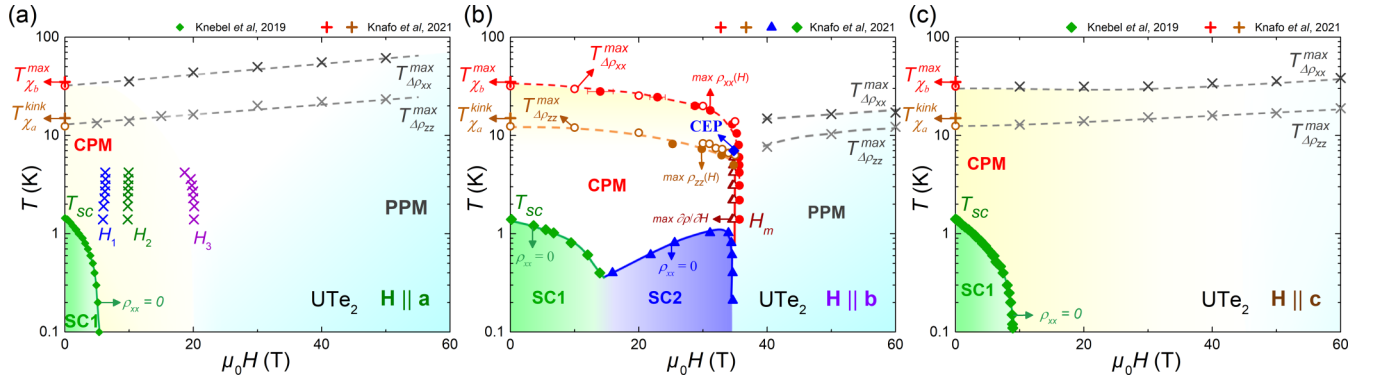


FIG. 4. Magnetic-field-temperature phase diagram of UTe_2 under a magnetic field: (a) $\mathbf{H} \parallel \mathbf{a}$, (b) $\mathbf{H} \parallel \mathbf{b}$, and (c) $\mathbf{H} \parallel \mathbf{c}$. CPM labels the correlated paramagnetic regime and PPM labels the polarized paramagnetic regime. SC1 labels the low-field superconducting phase and SC2 labels the superconducting phase induced by a magnetic field for $\mathbf{H} \parallel \mathbf{b}$. The superconducting boundaries correspond to the onset of zero resistivity and were extracted from Ref. [10] in the insets (a), (c), and from Ref. [13] in the inset of (b), where a scaling of the magnetic-field scale by a factor 1.02 was applied (to correct a small misorientation between the different sets of data).

and the enhancement of m^* is generally driven by magnetic fluctuations, consequence of nearby quantum magnetic instabilities. The electrical resistivity of UTe_2 , measured here at temperatures down to 1.4 K and in magnetic fields up to 70 T, was fitted by a Fermi-liquid formula for the six configurations of electrical current and magnetic field. Figure 5 shows Fermi-liquid fits to the data measured with $\mathbf{I} \parallel \mathbf{c}$ (details about the fits to the data with $\mathbf{I} \parallel \mathbf{a}$ can be found in the Supplementary Material of Ref. [8]). Depending on the magnetic-field direction and strength, the temperature window of the fit was adjusted from 4.2 K down to 1.4 K in the absence of superconductivity

and down to temperatures $> T_{SC}$ when superconductivity is established. Interestingly, within the experimental error of our pulsed field experiments, Fermi-liquid fits can be done near the metamagnetic field H_m for $\mathbf{H} \parallel \mathbf{b}$, where A is maximal for the two current directions.

Figure 6 presents the magnetic-field variations of A extracted for both current directions $\mathbf{I} \parallel \mathbf{a}$ and $\mathbf{I} \parallel \mathbf{c}$ and for the three magnetic-field directions $\mathbf{H} \parallel \mathbf{a}$, $\mathbf{H} \parallel \mathbf{b}$ and $\mathbf{H} \parallel \mathbf{c}$. The coefficient A is anisotropic and is an order magnitude larger for $\mathbf{I} \parallel \mathbf{c}$ than for $\mathbf{I} \parallel \mathbf{a}$. For $\mathbf{H} \parallel \mathbf{a}$ [Fig. 6(a)] and $\mathbf{H} \parallel \mathbf{c}$ [Fig. 6(c)], A decreases monotonously for both current

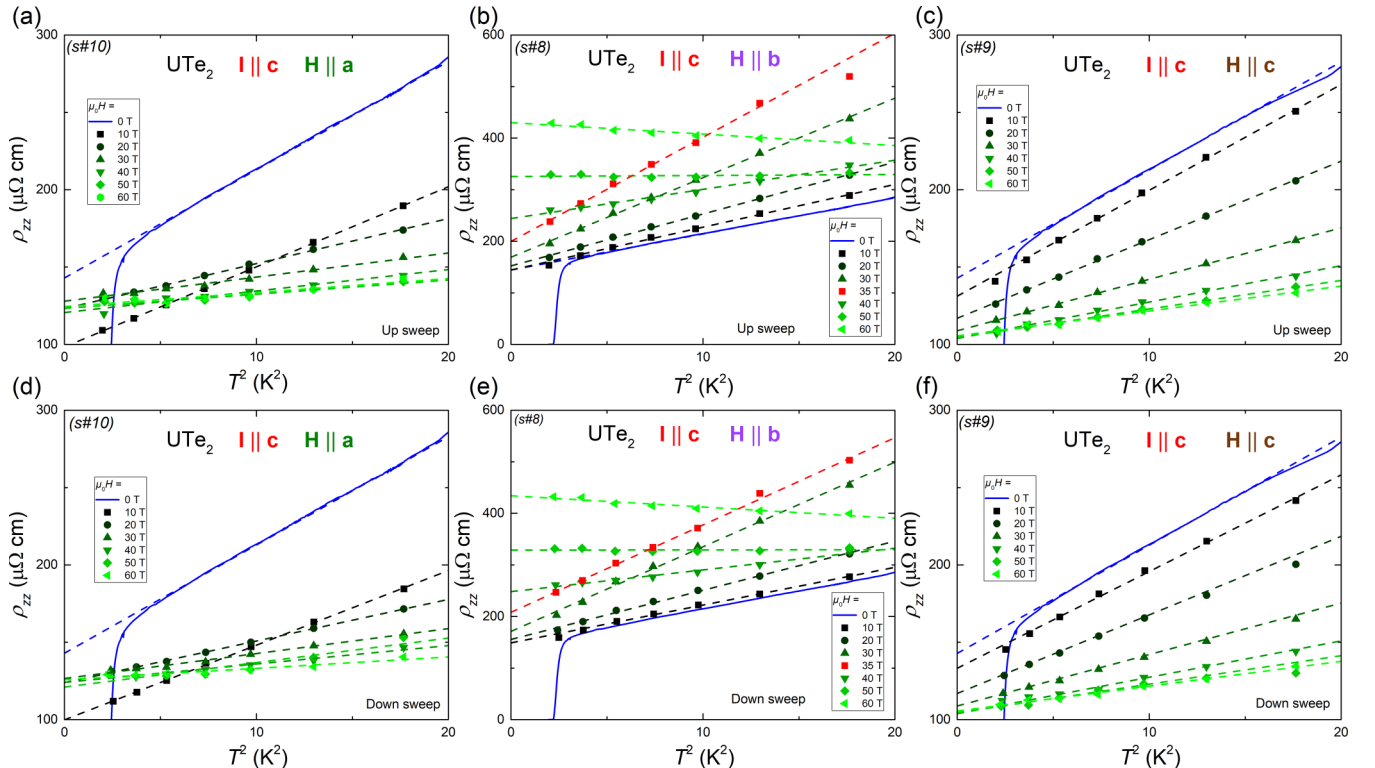


FIG. 5. Electrical resistivity ρ_{zz} , measured for $\mathbf{I} \parallel \mathbf{c}$, versus square of the temperature, and T^2 fits (dashed lines) to the data, for up-sweep with (a) $\mathbf{H} \parallel \mathbf{a}$, (b) $\mathbf{H} \parallel \mathbf{b}$, (c) $\mathbf{H} \parallel \mathbf{c}$, and down-sweep with (d) $\mathbf{H} \parallel \mathbf{a}$, (e) $\mathbf{H} \parallel \mathbf{b}$, (f) $\mathbf{H} \parallel \mathbf{c}$.

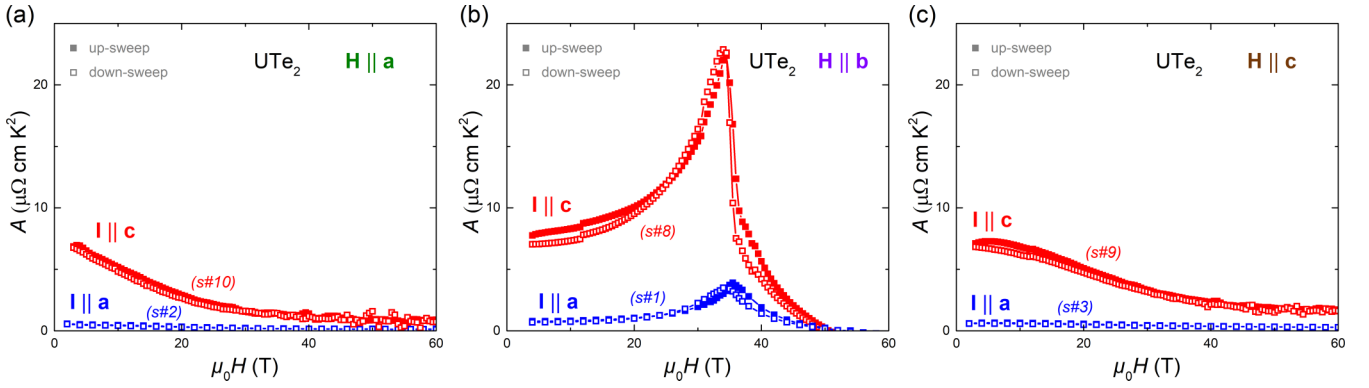


FIG. 6. Magnetic-field dependence of the quadratic coefficient A extracted using T^2 fits to the electrical resistivities ρ_{xx} and ρ_{zz} , measured respectively with currents $\mathbf{I} \parallel \mathbf{a}$ and $\mathbf{I} \parallel \mathbf{c}$, for (a) $\mathbf{H} \parallel \mathbf{a}$, (b) $\mathbf{H} \parallel \mathbf{b}$, and (c) $\mathbf{H} \parallel \mathbf{c}$.

directions. For $\mathbf{H} \parallel \mathbf{b}$, A presents a sharp maximum at H_m for both current directions. A striking difference between the two current-direction configurations is visible: the maximum in the field variation of A is symmetrical around H_m for $\mathbf{I} \parallel \mathbf{a}$ but A rapidly drops above H_m , by a factor 2 in a 2-T window, for $\mathbf{I} \parallel \mathbf{c}$ [see $A/A(H=0)$ plots in the Appendix]. The anisotropy of A , which is strong in the CPM regime for $H < H_m$, is reduced in the PPM regime for $H > H_m$. In the high-field limit, contributions controlled by field effects on the Fermi surface (for instance controlled by the field-induced cyclotron motion of carriers in transversal configurations) lead to deviations from a Fermi-liquid picture and to non-physical negative coefficients A .

IV. DISCUSSION

A. Energy scales of the electronic correlations

Two temperatures $T_{\Delta\rho_{xx}}^{\max} \simeq 32$ K and $T_{\Delta\rho_{zz}}^{\max} \simeq 12.5$ K characterizing the electronic correlations have been extracted from anomalies in the electrical resistivity with applied currents $\mathbf{I} \parallel \mathbf{a}$ and $\mathbf{I} \parallel \mathbf{c}$, respectively. A question is whether these characteristic energies are manifestations of one or two different phenomena. To address this question, a comparison with other physical quantities is of interest. We have seen that $T_{\Delta\rho_{xx}}^{\max}$ and $T_{\Delta\rho_{zz}}^{\max}$ coincide with the temperatures $T_{\chi_b}^{\max} \simeq 35$ K and $T_{\chi_a}^{\text{kink}} \simeq 15$ K, at which a maximum in the magnetic susceptibility χ_b measured with $\mathbf{H} \parallel \mathbf{b}$ and a kink in the magnetic susceptibility χ_a measured with $\mathbf{H} \parallel \mathbf{a}$ [15,28] (related with a minimum of $\partial\chi_a/\partial T$ [4]), are respectively observed. Anomalies are also visible in other physical quantities at these two temperature scales: a maximum in the electronic heat capacity, a minimum in the thermal expansion measured with lengths $\mathbf{L} \parallel \mathbf{b}, \mathbf{c}$ [41,42], and a minimum in the thermoelectric power measured with a current $\mathbf{I} \parallel \mathbf{a}$ [38] were observed at a temperature $\simeq 15$ K, while a maximum in the Hall effect measured with a current $\mathbf{I} \parallel \mathbf{a}$ and a magnetic field $\mathbf{H} \parallel \mathbf{b}$ was observed at a temperature $\simeq 35$ K [14,38]. These coincidences may support the picture of two characteristic temperatures related with two different energy scales.

We note that, in Ref. [42], it has been alternatively proposed that the magnetic susceptibility χ_a , the electronic heat capacity, and the thermal expansion should not be compared

to ρ_{xx} or ρ_{zz} , but to $\partial\rho_{xx}/\partial T$, where a maximum at $\simeq 15$ K is also observed. A single phenomenon, associated with the characteristic temperature of $\simeq 15$ K, was proposed to be relevant, the other temperatures scales being considered as onset temperatures of the phenomenon [43]. However, within this picture, a set of three energy scales, rather than a single one, may be needed to describe the transport and thermodynamic properties of UTe_2 : the first one of $\simeq 15$ K already identified, the second one of $\simeq 7$ K defined at the maximum of $\partial\rho_{zz}/\partial T$, and the third one of $\simeq 35$ K defined at the maximum of χ_b . In a recent NMR investigation [44], three temperatures scales were defined from the variation of the spin-spin-relaxation-rate $1/T_2$ measurements: $T_H = 30$ K at the onset of low-temperature increase of $1/T_2$, $T_P = 16$ K at a maximum of $1/T_2$, and $T_L = 7$ K at the onset of a lower-temperature increase of $1/T_2$. These three temperatures were proposed to be respectively related with the temperatures $T_{\chi_b}^{\max}$, T^* and a third temperature $T_\mu = 5$ K, below which the muon spin relaxation rate was found to increase [45].

In the following, we use the hypothesis of two energy scales associated with the characteristic temperatures of $\simeq 15$ K and $\simeq 35$ K identified here and we discuss their possible microscopic origin. Signatures of fluctuating magnetic moments $\mu \parallel \mathbf{a}$ associated with a characteristic temperature $T^* \simeq 15 - 20$ K were observed by NMR relaxation-rate measurements [33,44]. These fluctuations were found to develop progressively at temperatures below 30–40 K [44]. Inelastic-neutron-scattering experiments have further shown that antiferromagnetic fluctuations, peaked at the incommensurate wavevector $\mathbf{k}_1 = (0, 0.57, 0)$, saturate below a similar temperature $T_1^* \simeq 15$ K [28]. A quasi-two-dimensional (quasi-2D) character of the magnetic fluctuations was found and related with the low-dimensional structure of the magnetic U atoms in UTe_2 : two-legs ladders with legs along \mathbf{a} and rungs along \mathbf{c} , these ladders being weakly coupled along \mathbf{b} and not coupled along \mathbf{c} . These antiferromagnetic fluctuations may drive the anomalies at the first characteristic temperature of 15 K in a large set of physical properties, including ρ_{zz} investigated here.

The relation between $T_{\chi_b}^{\max} = 35$ K and the metamagnetic field $\mu_0 H_m = 35$ T was emphasized [8,9], indicating a standard heavy-fermion-paramagnet behavior [16,17]. In several prototypical heavy-fermion systems, T_χ^{\max} and H_m are the

boundaries (crossover or phase transition) delimiting a CPM regime, which is the place of antiferromagnetic fluctuations (see for instance CeRu₂Si₂ and CeCu₆ [46]). Therefore, in UTe₂ we expect that the second characteristic temperature of $\simeq 35$ K may be driven by antiferromagnetic fluctuations too. However, no magnetic-fluctuation mode with a temperature scale of $\simeq 35$ K was observed so far by inelastic neutron scattering. A few scenarios can be considered. Within a first scenario, quasi-1D magnetic fluctuations from noninteracting ladders, i.e., controlled only by the two nearest-distance interactions within the ladders, would progressively develop near $\simeq 35$ K. Quasi-1D fluctuations would then be transformed in quasi-2D fluctuations below 15 K, once the magnetic interaction between ladders would be activated. Within a second scenario, the 35-K anomaly may be related to a second magnetic-fluctuations mode with a different wave vector and/or a different moment direction. Within a third scenario, a single-site Kondo crossover would drive localized f electrons at temperatures $T > 35$ K to itinerant f electrons at temperatures $T \lesssim 35$ K (see proposition in Ref. [32]). Alternatively, within a fourth scenario, the low-temperature magnetic excitations at wave vector \mathbf{k}_1 , whose characteristic energy is of about 3 – 4 meV [28,29], were proposed to drive the 35 K anomaly in χ_b [29]. Understanding the relation between the temperature and energy scale of the two-dimensional magnetic fluctuations at wave vector \mathbf{k}_1 identified in Ref. [28] may help discriminating whether they drive the 15 K anomalies, as proposed here, or if they drive the 35-K anomalies, as proposed in Ref. [29]. New experiments are clearly needed to determine which description is pertinent.

B. Effect of a magnetic field

The fact that, in a magnetic field $\mathbf{H} \parallel \mathbf{b}$, $T_{\Delta\rho_{xx}}^{\max}$ and $T_{\Delta\rho_{zz}}^{\max}$ collapse in a similar manner when H_m is approached indicates that both are controlled by a common parameter [47]. The phenomenon associated with the 35-K temperature scale is a precursor of the phenomenon, identified here as quasi-2D antiferromagnetic fluctuations, associated with the 15-K temperature scale. This may be compatible with the first and third scenarios mentioned above. For $\mathbf{H} \parallel \mathbf{b}$ and $H > H_m$, the PPM regime is also characterized by broad maxima in $\Delta\rho_{xx}$ and $\Delta\rho_{zz}$ at the temperatures $T_{\Delta\rho_{xx}}^{\max}$ and $T_{\Delta\rho_{zz}}^{\max}$, respectively, which both then increase with H . For $\mathbf{H} \parallel \mathbf{a}$ and $\mathbf{H} \parallel \mathbf{c}$, there is no metamagnetic transition and $T_{\Delta\rho_{xx}}^{\max}$ and $T_{\Delta\rho_{zz}}^{\max}$ monotonously increase with H . The change from the CPM to the PPM regimes is then smooth and very progressive.

Under a magnetic field $\mathbf{H} \parallel \mathbf{b}$, the coefficient A passes through a maximum at H_m , indicating the presence of magnetic-field-induced critical magnetic fluctuations. The nature of these critical fluctuations is unknown. They could possibly be ferromagnetic, as observed at the metamagnetic transition of the heavy-fermion paramagnet CeRu₂Si₂ [48–50], or antiferromagnetic, as observed at the metamagnetic transition of Sr₃Ru₂O₇ [51]. The strong anisotropy of A , which is an order of magnitude larger for $\mathbf{I} \parallel \mathbf{c}$ than for $\mathbf{I} \parallel \mathbf{a}$ at zero field, indicates an anisotropic scattering process of the conduction electrons by the fluctuating magnetic moments. Interestingly, for $\mathbf{H} \parallel \mathbf{b}$ the field-variation of A measured with a current $\mathbf{I} \parallel \mathbf{c}$ has a similar asymmetric variation around H_m than the

field variation of the Sommerfeld coefficient extracted from heat-capacity measurements [11]. Therefore, the coefficient A from the configuration with $\mathbf{I} \parallel \mathbf{c}$ may capture the magnetic-fluctuations phenomena driving the entropy change near H_m .

The anisotropy of A is partly released in the PPM regime reached beyond H_m . For both current directions, a faster decrease of A observed for $\mathbf{H} \parallel \mathbf{a}$ than for $\mathbf{H} \parallel \mathbf{c}$ indicates a faster quench of the magnetic fluctuations. In relation with the decrease of A , the intensity of the resistivity anomalies in $\Delta\rho_{xx}$ and $\Delta\rho_{zz}$ decrease with H due to the field-induced quench of the magnetic fluctuations. This is consistent with the observation by magnetization measurements of a faster magnetic polarization for $\mathbf{H} \parallel \mathbf{a}$ than for $\mathbf{H} \parallel \mathbf{c}$ [39].

C. Perspectives

For a deeper understanding, a modeling of the contribution from magnetic fluctuations to electrical-transport properties is mandatory. Several theoretical studies have examined the contribution of magnetic fluctuations to the low-temperature resistivity regime. In an early work from Mills and Lederer, the contribution to the electrical resistivity, via $s-d$ exchange, of magnetic fluctuations from localized electrons was modeled and was shown to lead to a T^2 Fermi-liquid behavior [52]. A bit later, Jullien, Béal-Monod, and Coqblin described the contribution from magnetic fluctuations to the electrical resistivity over a broad temperature range [53]. Further works analyzed the dominant contribution of critical magnetic fluctuations near a quantum magnetic phase transition at low temperatures, leading to a non-Fermi-liquid behavior in the electrical resistivity (see for instance Refs. [54]). The effect of disorder and of Fermi-surface hot spots in nearly antiferromagnets was also emphasized [55]. These approaches were however essentially done for isotropic cases. The challenge to reproduce the anisotropic features reported in the electrical resistivity and in the magnetic susceptibility of UTe₂ requires a new generation of modeling, possibly based on anisotropic Kondo hybridization processes [56], and taking into account the magnetic and Fermi-surface anisotropies. In particular, we have seen here that, at ambient pressure, ρ_{zz} seems to capture the 15-K anomaly revealed in χ_a , while ρ_{xx} seems to capture the 35-K anomaly revealed in χ_b . Under pressures higher than the critical pressure $p_c \simeq 1.5 - 1.7$ GPa, it was also shown that ρ_{xx} captures an anomaly at $\simeq 15 - 20$ K, which is possibly related with maxima in χ_a or in χ_c [23,26,57]. The possibility to quantitatively, or at least qualitatively, describe the anisotropic contributions from the magnetic fluctuations to the electrical resistivity may be useful to understand their relationship with the stabilization of multiple unconventional superconducting phases in UTe₂. Indeed, magnetic fluctuations are suspected to contribute to the superconducting pairing mechanisms in UTe₂, and magnetic-field- or pressure-induced modifications of the nature and strength of the magnetic fluctuations may be related to the stabilization or destabilization of the superconducting phases. The anisotropy of the critical field H_{c2} of the low-field superconducting phase SC1 was found to be inversely related with the anisotropy of the low-temperature magnetic susceptibility [13]: for instance, for $\mathbf{H} \parallel \mathbf{a}$, H_{c2} is minimal and the low-temperature magnetic susceptibility χ

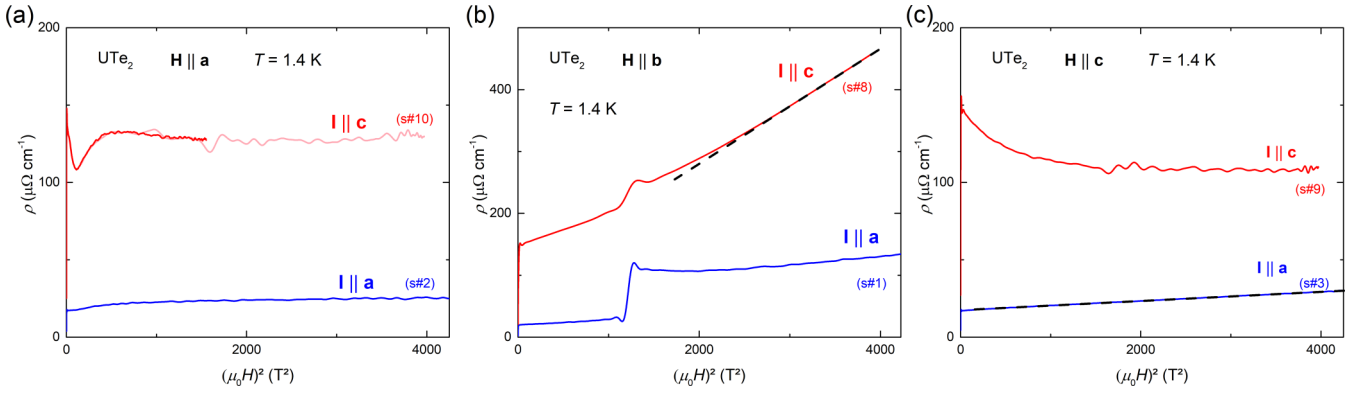


FIG. 7. Electrical resistivities ρ_{xx} and ρ_{zz} , measured with currents $\mathbf{I} \parallel \mathbf{a}$ and $\mathbf{I} \parallel \mathbf{c}$, respectively, of UTe_2 versus square of the magnetic field H^2 at the temperature $T = 1.4 \text{ K}$ under magnetic fields (a) $\mathbf{H} \parallel \mathbf{a}$, (b) $\mathbf{H} \parallel \mathbf{b}$, (c) $\mathbf{H} \parallel \mathbf{c}$. Dashed lines indicates H^2 variations observed for the configurations $\mathbf{I} \parallel \mathbf{c}, \mathbf{H} \parallel \mathbf{b}$ and $\mathbf{I} \parallel \mathbf{a}, \mathbf{H} \parallel \mathbf{c}$.

is maximal, the magnetic polarization is faster (evidenced from magnetization measurements [9,39]) and the quench of the low-temperature contribution to ρ_{zz} and ρ_{xx} is reached at lower fields. These phenomena are presumably related to the fast quench of magnetic fluctuations. The anisotropic variation of the coefficient A in a magnetic field $\mathbf{H} \parallel \mathbf{b}$ is also presently unexplained and may result from peculiar field-induced variations of the magnetic excitation spectrum, with possible feedback to superconductivity. The modeling of the magnetic fluctuations and their anisotropic contributions to the electrical resistivity of a real crystal, as the unconventional superconductor UTe_2 studied here, may request considering the anisotropy of the electronic bands and constitutes a theoretical challenge for the coming years.

ACKNOWLEDGMENTS

We acknowledge financial support from the French National Research Agency collaborative research project FRESKO No. ANR-20-CE30-0020, from the JSPS KAKENHI Grants No. JP19H00646, No. 19K03756, No. 20H00130, No. 20H01864, No. JP20K20889, No. JP20KK0061, and No. 21H04987, by the Czech Science Foundation (GAČR), project No. 22-22322S.

APPENDIX

In this Appendix, we present complementary graphs about the electrical-resistivity data accumulated for this study. Details about the construction of the phase diagrams, the variations of the Fermi-liquid coefficient A , and about the resistivity background estimation are given.

1. Contribution to the electrical resistivity from field-induced motion of carriers

Figure 7 presents plots of the electrical resistivity ρ versus the square of the magnetic field H^2 at $T = 1.4 \text{ K}$, for both current directions $\mathbf{I} \parallel \mathbf{a}$ and $\mathbf{I} \parallel \mathbf{c}$ and the three field directions $\mathbf{H} \parallel \mathbf{a}$ [Inset (a)], $\mathbf{H} \parallel \mathbf{b}$ [Inset (b)], $\mathbf{H} \parallel \mathbf{c}$ [Inset (c)]. A high-field H^2 variation of the electrical resistivity is observed for the two transverse configurations $\mathbf{I} \parallel \mathbf{c}, \mathbf{H} \parallel \mathbf{b}$ and $\mathbf{I} \parallel \mathbf{a}, \mathbf{H} \parallel \mathbf{c}$. A high-field increase of the electrical resistivity, which

does not follow a H^2 law, is also observed for the transverse configuration $\mathbf{I} \parallel \mathbf{a}, \mathbf{H} \parallel \mathbf{b}$.

Knowing that UTe_2 is a compensated metal and assuming that cylindrical Fermi surfaces along the direction \mathbf{c} dominate the high-field electrical resistivity [34–36], one can expect H^2 variations for certain transverse magnetic-field and electrical-current configurations [58]:

(1) For $\mathbf{H} \parallel \mathbf{c}$, cyclotron orbits have their axis $\parallel \mathbf{H}$ and appear as closed orbits. In a high magnetic field, the contribution from carriers to the resistivity in the transverse configurations with $\mathbf{I} \parallel \mathbf{a}, \mathbf{b}$ is expected to follow a H^2 law, while that in the longitudinal configuration with $\mathbf{I} \parallel \mathbf{c}$ is expected to saturate.

(2) For $\mathbf{H} \perp \mathbf{c}$, cyclotron orbits appear as open orbits. In a high magnetic field, the contribution from carriers to the resistivity in the transverse configuration with $\mathbf{I} \parallel \mathbf{c}$ is expected to follow a H^2 law, while that in the transverse and longitudinal configurations with $\mathbf{I} \perp \mathbf{c}$ are expected to saturate.

Table I summarizes the behaviors expected for cylindrical Fermi surfaces and those observed here for UTe_2 . Four of the six considered configurations indicate that a first approximation of cylindrical Fermi surfaces seems appropriate for UTe_2 . However, deviations from the two-dimensional cylindrical case are found for two configurations: for $\mathbf{H} \parallel \mathbf{a}$ and $\mathbf{I} \parallel \mathbf{c}$, where the resistivity saturates, and for $\mathbf{H} \parallel \mathbf{b}$ and $\mathbf{I} \parallel \mathbf{a}$, where the resistivity slightly increases. These differences may be due to a three-dimensional character, i.e., a nonperfectly cylindrical shape, of the Fermi surfaces dominating the high-field resistivity of UTe_2 .

2. Anomalies at the magnetic fields H_1, H_2, H_3 , and H_m

Figure 8 shows a zoom on the magnetic-field dependence of the electrical resistivities ρ_{xx} and ρ_{zz} , measured with currents $\mathbf{I} \parallel \mathbf{a}$ and $\mathbf{I} \parallel \mathbf{c}$, respectively, at temperatures $T \leq 5 \text{ K}$ and magnetic fields $\mu_0 H \leq 30 \text{ T}$ applied along \mathbf{a} . Signatures of magnetic crossover are observed at the fields $\mu_0 H_1 \simeq 6 \text{ T}$, $\mu_0 H_2 \simeq 10 \text{ T}$ and $\mu_0 H_3 \simeq 20 \text{ T}$, in agreement with a previous report where they were attributed to Fermi-surface reconstructions [38], while only a broad kink is observed at H_2 for $\mathbf{I} \parallel \mathbf{a}$. The trace of these anomalies is lost when the temperature is increased beyond 5 K .

TABLE I. High-field resistivity for different magnetic-field and electrical-current configurations, expected for a cylindrical Fermi surface [58] and observed here for UTe₂.

Magnetic field	Electrical current	Expected for a cylindrical Fermi surface	Observed for UTe ₂
H ∥ a	I ∥ a	Saturation	Saturation
	I ∥ b	Saturation	(not measured)
	I ∥ c	H^2	Saturation
H ∥ b	I ∥ a	Saturation	Small increase
	I ∥ b	Saturation	(not measured)
	I ∥ c	H^2	H^2
H ∥ c	I ∥ a	H^2	H^2
	I ∥ b	H^2	(not measured)
	I ∥ c	Saturation	Saturation

Figure 9 presents details concerning the determination of the metamagnetic field H_m for **H** ∥ **b**. The first-order character of the transition is indicated by an extremum of the field-derivative of the electrical resistivity, at which H_m is defined, and by an hysteresis. For **I** ∥ **c**, we lose the signatures of the first-order transition at temperatures beyond 6 K, where the critical endpoint can be defined. For **I** ∥ **a**, we lose the signatures of the first-order transition at temperatures beyond 7 K, where the critical endpoint can be defined. The differences in the temperature dependences of the hysteresis at H_m may result from deviations from isothermal conditions in the two setups, due to Eddy currents and magnetocaloric effect in the samples. Such deviations may differ for the two configurations, in relation with different geometries of the samples and different couplings to the sapphire sample holder.

3. Fermi-liquid fits to the data

Figure 10 presents complementary plots of the variations with field of the coefficient A normalized by its zero field value. These graphs emphasize the different fields variations of $A/A(H=0)$ for the two current directions **I** ∥ **a** and **I** ∥ **c**, in a magnetic field **H** ∥ **b**. For the two field directions **H** ∥ **a** and **H** ∥ **c**, similar decreases of $A/A(H=0)$ are observed for the two current directions.

Nonphysical negative coefficients A are obtained in high fields for the two transversal configurations measured with

H ∥ **b**, where a low-temperature increase of the resistivity at high field is presumably driven by cyclotron motion of the carriers. However, these deviations are smooth in the vicinity of H_m , and we can safely conclude that the variations of A near H_m are mainly controlled by the quantum critical properties. We note that small deviations from an isothermal condition induced by the combination of magnetocaloric effect and eddy-currents heating, may be responsible for the differences near H_m between up and down sweep variations of the electrical resistivity, and then of the A coefficient extracted here.

4. Estimation of a background for the electrical-resistivity data

In many heavy-fermion paramagnets, the temperature T_χ^{\max} and the metamagnetic field H_m delimitate a CPM regime, where magnetic correlations lead to magnetic fluctuations whose characteristic energy scale is the relaxation rate Γ (see Refs. [16,17]). The three quantities can be related by an universal law $T_\chi^{\max} \propto H_m \propto \Gamma$, which indicates that they are controlled by a unique phenomenon, presumably antiferromagnetic correlations of relaxation rate Γ . In CeCu₆ and CeRu₂Si₂, the observation that antiferromagnetic fluctuations vanish beyond H_m [46] confirms that they are intrinsic to the CPM regime.

In UTe₂, the temperature scales of $\simeq 30$ K and $\simeq 12.5$ K, below which maxima in $\rho_{xx}(H)$ and $\rho_{zz}(H)$, respectively, are

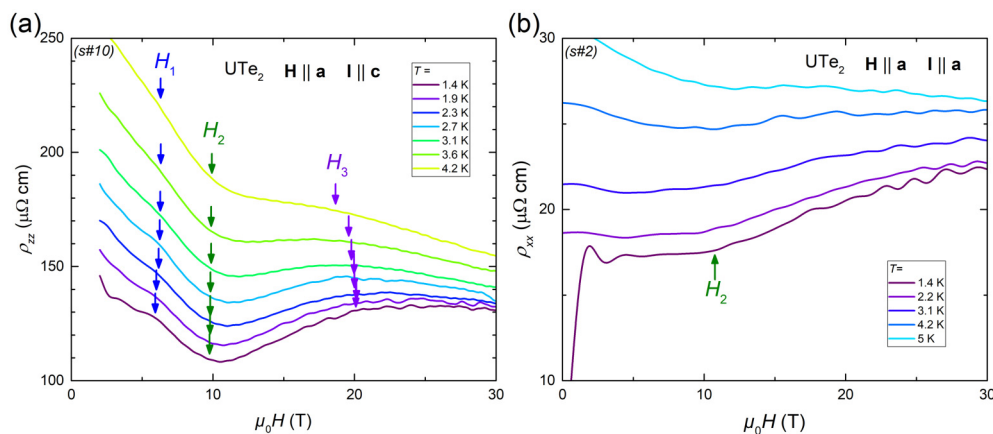


FIG. 8. Magnetic-field dependence of the electrical resistivities (a) ρ_{xx} and (b) ρ_{zz} , measured with currents **I** ∥ **a** and **I** ∥ **c**, respectively, at temperatures $T \leq 5$ K and magnetic fields $\mu_0H \leq 30$ T applied along **a**.

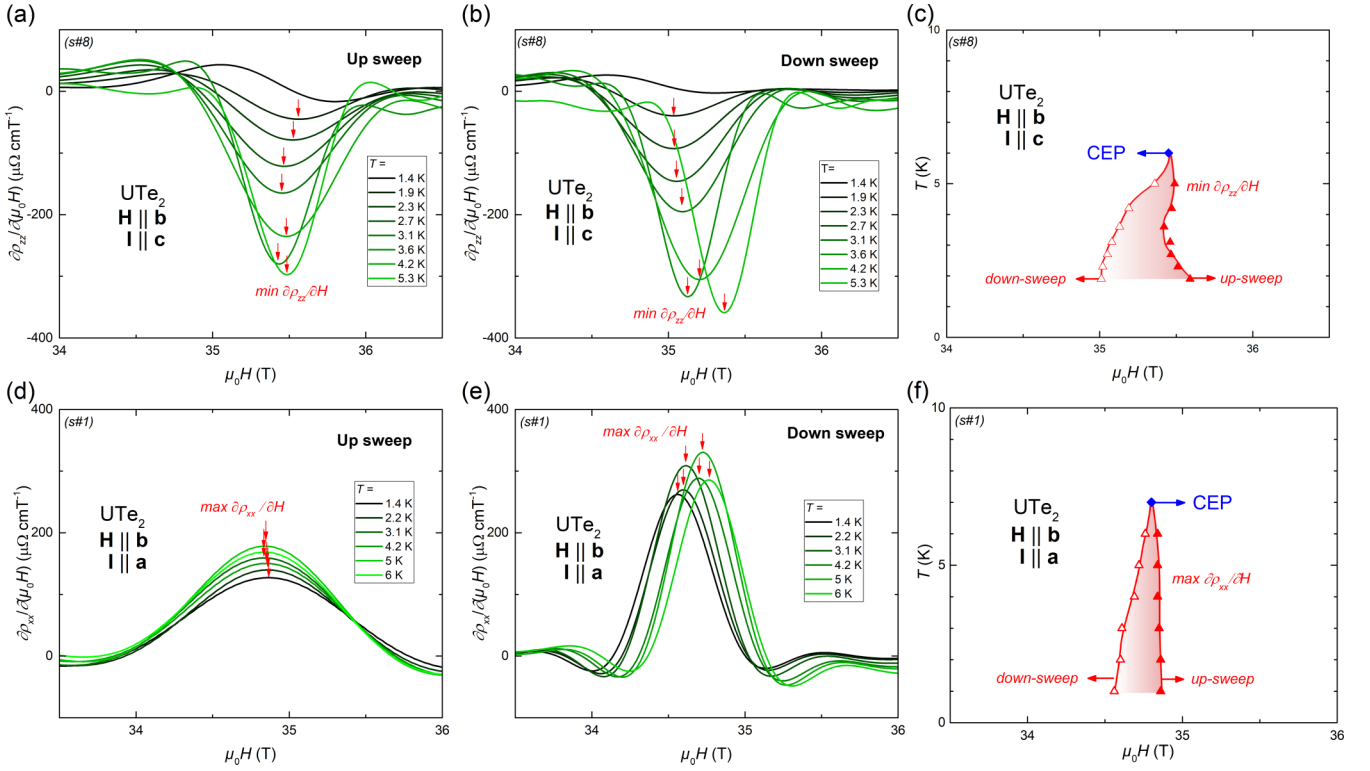


FIG. 9. Field-derivative of the electrical resistivity $\partial\rho_{zz}/\partial H$ versus magnetic field $\mathbf{H} \parallel \mathbf{b}$ measured for $\mathbf{I} \parallel \mathbf{c}$ at temperatures $T \leq 5.3$ K: (a) up-sweep and (b) down-sweep, and (c) corresponding magnetic-field-temperature phase diagram showing the hysteresis at H_m , and field-derivative of the electrical resistivity $\partial\rho_{xx}/\partial H$ versus magnetic field measured $\mathbf{H} \parallel \mathbf{b}$ for $\mathbf{I} \parallel \mathbf{a}$ at temperatures $T \leq 6$ K: (d) up-sweep and (e) down-sweep, and (f) corresponding magnetic-field-temperature phase diagram showing the hysteresis at H_m .

observed, have been extracted without background subtraction. Since the first temperature scale of 30 K of the electrical resistivity coincides with $T_{\chi}^{\max} = 35$ K, we identify it as a signature of the boundary of the CPM regime. We also suspect that the anomalies in ρ_{xx} characterizing the CPM regime may be driven by antiferromagnetic fluctuations, as in other heavy-fermion systems. The phenomena driving to maxima in $\rho(H)$ also drive to contributions in $\rho(T)$. However, due to additional T -dependent (but not, or weakly, H -dependent) contributions, an anomaly in $\rho(T)$ either has a maximum shifted to higher temperatures [in comparison with the H - T phase diagram determined from $\rho(H)$ data], or can be characterized by a broad

shoulder without maximum. The subtraction of a background is therefore needed to identify the characteristic temperatures from $\rho(T)$ data. Here, based on the assumption that the magnetic fluctuations, and thus the associated anomalies in the low-field resistivity, collapse in the PPM regime, we estimate resistivity backgrounds using data collected deep inside the high-field PPM regime, either at ambient pressure or under pressure. For that purpose, Fig. 11 compares the temperature dependences of the electrical resistivities ρ_{zz} with $\mathbf{I} \parallel \mathbf{c}$ and ρ_{xx} with $\mathbf{I} \parallel \mathbf{a}$ measured at zero field and in a magnetic field of 60 T for the three directions of field $\mathbf{H} \parallel \mathbf{a}$, $\mathbf{H} \parallel \mathbf{b}$, and $\mathbf{H} \parallel \mathbf{c}$, and at 49 T for $\mathbf{I} \parallel \mathbf{a}$, $\mathbf{H} \parallel \mathbf{b}$ within a pressure $p = 2.25$ GPa.

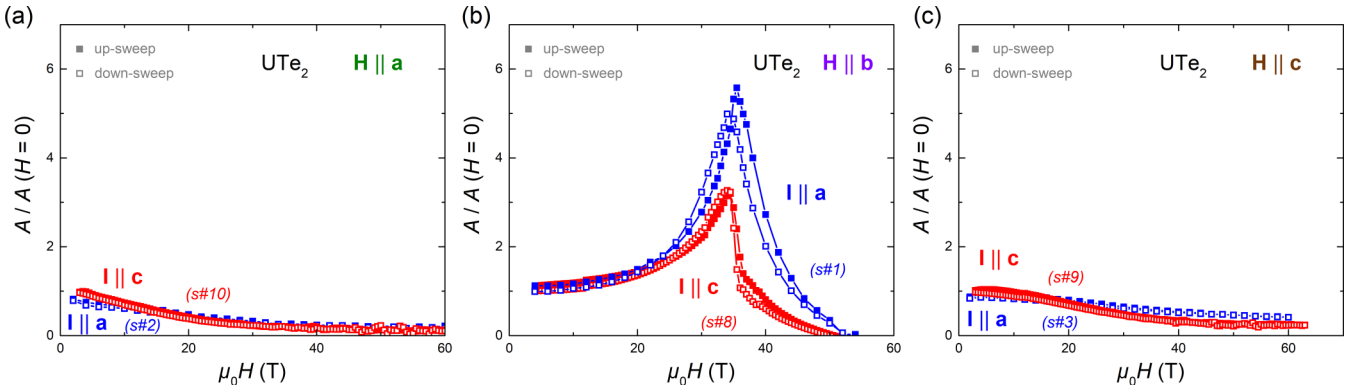


FIG. 10. Magnetic-field dependence of normalized quadratic coefficient $A/A(H=0)$ extracted using T^2 fits to the electrical resistivities ρ_{xx} and ρ_{zz} , measured, respectively, with currents $\mathbf{I} \parallel \mathbf{a}$ and $\mathbf{I} \parallel \mathbf{c}$, for (a) $\mathbf{H} \parallel \mathbf{a}$, (b) $\mathbf{H} \parallel \mathbf{b}$, and (c) $\mathbf{H} \parallel \mathbf{c}$.

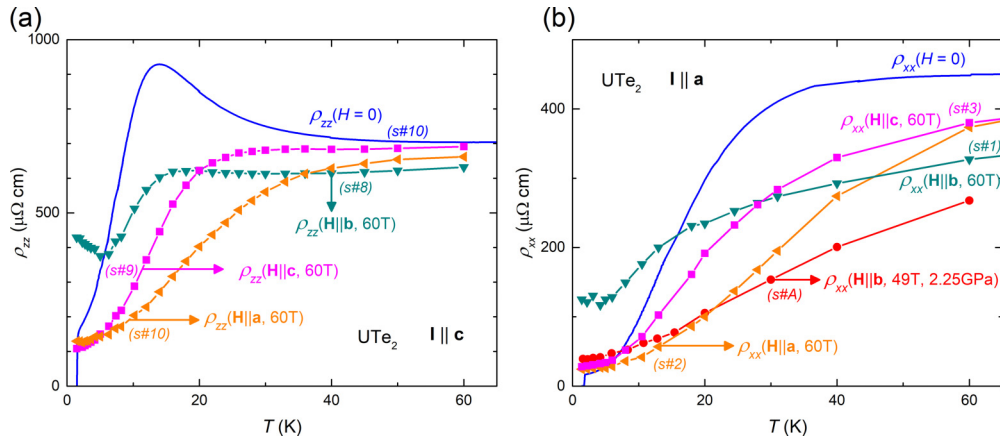


FIG. 11. (a) Electrical resistivity ρ_{zz} , measured for $\mathbf{I} \parallel \mathbf{c}$, versus temperature, for $H = 0$ and $\mu_0 H = 60$ T applied along \mathbf{a} , \mathbf{b} , and \mathbf{c} . (b) Electrical resistivity ρ_{xx} , measured for $\mathbf{I} \parallel \mathbf{a}$, versus temperature, for $H = 0$, $\mu_0 H = 60$ T applied along \mathbf{a} , \mathbf{b} , and \mathbf{c} , and for $\mu_0 H = 60$ T applied along \mathbf{b} at the pressure $p = 2.25$ GPa.

In the configuration with $\mathbf{I} \parallel \mathbf{c}$, all high-field resistivity data were measured at ambient pressure. We find that $\rho_{zz}(\mathbf{H} \parallel \mathbf{a}, 60 \text{ T})$ corresponds to the smallest measured resistivity in the temperature range [1.5–60 K] considered here. In this configuration, the low-temperature anomaly reported at $\simeq 15$ K at zero field has almost completely vanished. Knowing that the magnetization saturates beyond 20 T at low temperature when the magnetic field is applied along the easy magnetic axis \mathbf{a} [9,39], we can reasonably infer that most of the low-temperature electronic correlations, including the magnetic fluctuations, have been quenched by a magnetic field of 60 T applied along \mathbf{a} , and thus that $\rho_{zz}(\mathbf{H} \parallel \mathbf{a}, 60 \text{ T})$ can be used as background. By subtracting $\rho_{zz}(\mathbf{H} \parallel \mathbf{a}, 60 \text{ T})$ from the data, we determine a temperature scale $T_{\Delta\rho_{zz}}^{\max} = 12.5$ K, which coincides with the temperature of 12.5 K below which a maximum in $\rho_{zz}(H)$ is observed. $T_{\Delta\rho_{zz}}^{\max}$ is smaller than the temperature of $\simeq 14$ K at which $\rho_{zz}(T)$ is maximum. This confirms the pertinence of the background estimated here. We note that, for $\mathbf{H} \parallel \mathbf{c}$ the magnetization is not fully polarized at 60 T at low temperature [39], and a contribution to the electrical resistivity $\rho_{zz}(\mathbf{H} \parallel \mathbf{c}, 60 \text{ T})$ is visible at $\simeq 20$ K, indicating that part of the magnetic fluctuations has not been quenched.

In the configuration with $\mathbf{I} \parallel \mathbf{a}$, high-field data were extracted at ambient pressure for the field directions $\mathbf{H} \parallel \mathbf{a}$, \mathbf{b} , \mathbf{c} and under pressure for $\mathbf{H} \parallel \mathbf{b}$ [26]. We find that $\rho_{xx}(\mathbf{H} \parallel \mathbf{b}, 49 \text{ T}, 2.25 \text{ GPa})$ measured for $\mu_0 H = 49$ T applied along \mathbf{b} and at the pressure $p = 2.25$ GPa is smaller than $\rho_{xx}(\mathbf{H} \parallel \mathbf{a}, 60 \text{ T})$ measured in a magnetic field $\mu_0 \mathbf{H} \parallel \mathbf{a}$ of 60 T. The configuration under pressure offers a better estimation of the background in the temperature range [1.5–80 K] considered here. The magnetization was not measured in this high-field and high-pressure configuration but we can reasonably expect that it corresponds to a state deep inside the PPM regime, where most of the magnetic fluctuations have vanished. Indeed, the metamagnetic field has then vanished down to < 15 T [19,26] and the magnetic susceptibility is enhanced in comparison with ambient pressure susceptibility [23]. This indicates that a PPM regime is expected to be reached at much lower fields than at ambient pressure. By using $\rho_{xx}(\mathbf{H} \parallel \mathbf{b}, 49 \text{ T}, 2.25 \text{ GPa})$ as background, we determine a temperature scale $T_{\Delta\rho_{xx}}^{\max} = 32$ K which coincides with the temperature of 30 K below which a maximum in $\rho_{xx}(H)$ is observed. $T_{\Delta\rho_{xx}}^{\max}$ is twice smaller than the temperature of $\simeq 65$ K at which $\rho_{zz}(T)$ is maximum. This confirms the pertinence of the background estimated here.

- [1] P. Monthoux, D. Pines, and G. Lonzarich, *Nature (London)* **450**, 1177 (2007).
- [2] S. Ran, C. Eckberg, Q.-P. Ding, Y. Furukawa, T. Metz, S. R. Saha, I.-L. Liu, M. Zic, H. Kim, J. Paglione, and N. P. Butch, *Science* **365**, 684 (2019).
- [3] D. Aoki, A. Nakamura, F. Honda, D. Li, Y. Homma, Y. Shimizu, Y. J. Sato, G. Knebel, J.-P. Brison, A. Pourret, D. Braithwaite, G. Lapertot, Q. Niu, M. Vališka, H. Harima, and J. Flouquet, *J. Phys. Soc. Jpn.* **88**, 043702 (2019).
- [4] D. Aoki, J.-P. Brison, J. Flouquet, K. Ishida, G. Knebel, Y. Tokunaga, and Y. Yanase, *J. Phys.: Condens. Matter* **34**, 243002 (2022).
- [5] S. Ran, I.-L. Liu, Y. S. Eo, D. J. Campbell, P. Neves, W. T. Fuhrman, S. R. Saha, C. Eckberg, H. Kim, J. Paglione, D. Graf, J. Singleton, and N. P. Butch, *Nat. Phys.* **15**, 1250 (2019).
- [6] G. Nakamine, S. Kitagawa, K. Ishida, Y. Tokunaga, H. Sakai, S. Kambe, A. Nakamura, Y. Shimizu, Y. Homma, D. Li, F. Honda, and D. Aoki, *J. Phys. Soc. Jpn.* **88**, 113703 (2019).
- [7] H. Fujibayashi, G. Nakamine, K. Kinjo, S. Kitagawa, K. Ishida, Y. Tokunaga, H. Sakai, S. Kambe, A. Nakamura, Y. Shimizu, Y. Homma, D. Li, F. Honda, and D. Aoki, *J. Phys. Soc. Jpn.* **91**, 043705 (2022).
- [8] W. Knafo, M. Vališka, D. Braithwaite, G. Lapertot, G. Knebel, A. Pourret, J.-P. Brison, J. Flouquet, and D. Aoki, *J. Phys. Soc. Jpn.* **88**, 063705 (2019).
- [9] A. Miyake, Y. Shimizu, Y. J. Sato, D. Li, A. Nakamura, Y. Homma, F. Honda, J. Flouquet, M. Tokunaga, and D. Aoki, *J. Phys. Soc. Jpn.* **88**, 063706 (2019).
- [10] G. Knebel, W. Knafo, A. Pourret, Q. Niu, M. Vališka, D. Braithwaite, G. Lapertot, M. Nardone, A. Zitouni, S. Mishra,

- I. Sheikin, G. Seyfarth, J.-P. Brison, D. Aoki, and J. Flouquet, *J. Phys. Soc. Jpn.* **88**, 063707 (2019).
- [11] A. Rosuel, C. Marcenat, G. Knebel, T. Klein, A. Pourret, N. Marquardt, Q. Niu, S. Rousseau, A. Demuer, G. Seyfarth, G. Lapertot, D. Aoki, D. Braithwaite, J. Flouquet, and J.-P. Brison, [arXiv:2205.04524](https://arxiv.org/abs/2205.04524).
- [12] W. C. Lin, D. J. Campbell, S. Ran, I.-L. Liu, H. Kim, A. H. Nevidomskyy, D. Graf, N. P. Butch, and J. Paglione, *npj Quantum Mater.* **5**, 68 (2020).
- [13] W. Knafo, M. Nardone, M. Vališka, A. Zitouni, G. Lapertot, D. Aoki, G. Knebel, and D. Braithwaite, *Commun. Phys.* **4**, 40 (2021).
- [14] Q. Niu, G. Knebel, D. Braithwaite, D. Aoki, G. Lapertot, M. Vališka, G. Seyfarth, W. Knafo, T. Helm, J.-P. Brison, J. Flouquet, and A. Pourret, *Phys. Rev. Res.* **2**, 033179 (2020).
- [15] S. Ikeda, H. Sakai, D. Aoki, Y. Homma, E. Yamamoto, A. Nakamura, Y. Shiokawa, Y. Haga, and Y. Ōnuki, *J. Phys. Soc. Jpn.* **75**, 116 (2006).
- [16] D. Aoki, W. Knafo, and I. Sheikin, *C. R. Phys.* **14**, 53 (2013).
- [17] W. Knafo, [arXiv:2107.13458](https://arxiv.org/abs/2107.13458).
- [18] D. Braithwaite, M. Vališka, G. Knebel, G. Lapertot, J.-P. Brison, A. Pourret, M. E. Zhitomirsky, J. Flouquet, F. Honda, and D. Aoki, *Commun. Phys.* **2**, 147 (2019).
- [19] G. Knebel, M. Kimata, M. Vališka, F. Honda, D. Li, D. Braithwaite, G. Lapertot, W. Knafo, A. Pourret, Y. J. Sato, Y. Shimizu, T. Kihara, J.-P. Brison, J. Flouquet, and D. Aoki, *J. Phys. Soc. Jpn.* **89**, 053707 (2020).
- [20] S. Ran, H. Kim, I.-L. Liu, S. R. Saha, I. Hayes, T. Metz, Y. S. Eo, J. Paglione, and N. P. Butch, *Phys. Rev. B* **101**, 140503(R) (2020).
- [21] S. M. Thomas, F. B. Santos, M. H. Christensen, T. Asaba, F. Ronning, J. D. Thompson, E. D. Bauer, R. M. Fernandes, G. Fabbris, and P. F. S. Rosa, *Sci. Adv.* **6**, eabc8709 (2020).
- [22] D. Aoki, F. Honda, G. Knebel, D. Braithwaite, A. Nakamura, D. Li, Y. Homma, Y. Shimizu, Y. J. Sato, J.-P. Brison, and J. Flouquet, *J. Phys. Soc. Jpn.* **89**, 053705 (2020).
- [23] D. Li, A. Nakamura, F. Honda, Y. J. Sato, Y. Homma, Y. Shimizu, J. Ishizuka, Y. Yanase, G. Knebel, J. Flouquet, and D. Aoki, *J. Phys. Soc. Jpn.* **90**, 073703 (2021).
- [24] S. Ran, S. R. Saha, I.-L. Liu, D. Graf, J. Paglione, and N. P. Butch, *npj Quantum Mater.* **6**, 75 (2021).
- [25] D. Aoki, M. Kimata, Y. J. Sato, G. Knebel, F. Honda, A. Nakamura, D. Li, Y. Homma, Y. Shimizu, W. Knafo, D. Braithwaite, M. Vališka, A. Pourret, J.-P. Brison, and J. Flouquet, *J. Phys. Soc. Jpn.* **90**, 074705 (2021).
- [26] M. Vališka, W. Knafo, G. Knebel, G. Lapertot, D. Aoki, and D. Braithwaite, *Phys. Rev. B* **104**, 214507 (2021).
- [27] C. Duan, K. Sasmal, M. B. Maple, A. Podlesnyak, J.-X. Zhu, Q. Si, and P. Dai, *Phys. Rev. Lett.* **125**, 237003 (2020).
- [28] W. Knafo, G. Knebel, P. Steffens, K. Kaneko, A. Rosuel, J.-P. Brison, J. Flouquet, D. Aoki, G. Lapertot, and S. Raymond, *Phys. Rev. B* **104**, L100409 (2021).
- [29] N. P. Butch, S. Ran, S. R. Saha, P. M. Neves, M. P. Zic, J. Paglione, S. Gladchenko, Q. Ye, and J. A. Rodriguez, *npj Quantum Mater.* **7**, 39 (2022).
- [30] C. Duan, R. Baumbach, A. Podlesnyak, Y. Deng, C. Moir, A. J. Breindel, M. B. Maple, E. Nica, Q. Si, and P. Dai, *Nature (London)* **600**, 636 (2021).
- [31] S. Raymond, W. Knafo, G. Knebel, K. Kaneko, J.-P. Brison, J. Flouquet, D. Aoki, and G. Lapertot, *J. Phys. Soc. Jpn.* **90**, 113706 (2021).
- [32] Y. S. Eo, S. R. Saha, H. Kim, S. Ran, J. A. Horn, H. Hodovanets, J. Collini, W. T. Fuhrman, A. H. Nevidomskyy, N. P. Butch, M. S. Fuhrer, and J. Paglione, *Phys. Rev. B* **106**, L060505 (2022).
- [33] Y. Tokunaga, H. Sakai, S. Kambe, T. Hattori, N. Higa, G. Nakamine, S. Kitagawa, K. Ishida, A. Nakamura, Y. Shimizu, Y. Homma, D. Li, F. Honda, and D. Aoki, *J. Phys. Soc. Jpn.* **88**, 073701 (2019).
- [34] Y. Xu, Y. Sheng, and Y.-F. Yang, *Phys. Rev. Lett.* **123**, 217002 (2019).
- [35] J. Ishizuka, S. Sumita, A. Daido, and Y. Yanase, *Phys. Rev. Lett.* **123**, 217001 (2019).
- [36] L. Miao, S. Liu, Y. Xu, E. C. Kotta, C.-J. Kang, S. Ran, J. Paglione, G. Kotliar, N. P. Butch, J. D. Denlinger, and L. A. Wray, *Phys. Rev. Lett.* **124**, 076401 (2020).
- [37] G. Knebel (private communication).
- [38] Q. Niu, G. Knebel, D. Braithwaite, D. Aoki, G. Lapertot, G. Seyfarth, J.-P. Brison, J. Flouquet, and A. Pourret, *Phys. Rev. Lett.* **124**, 086601 (2020).
- [39] A. Miyake, Y. Shimizu, Y. J. Sato, D. Li, A. Nakamura, Y. Homma, F. Honda, J. Flouquet, M. Tokunaga, and D. Aoki, *J. Phys. Soc. Jpn.* **90**, 103702 (2021).
- [40] The pertinence of the background subtractions done here is supported by the findings (i) that the fields at the maxima of ρ_{zz} versus H extracted at constant temperatures coincide with the temperatures $T_{\Delta\rho_{zz}}^{\max}$ at the maxima of $\Delta\rho_{zz}$ versus T extracted at constant fields and (ii) that the fields at the maxima of ρ_{xx} versus H extracted at constant temperatures coincide with the temperatures $T_{\Delta\rho_{xx}}^{\max}$ at the maxima of $\Delta\rho_{xx}$ versus T extracted at constant fields (see phase diagrams in Fig. 4). A similar background-subtraction procedure was done to analyze ρ_{xx} data measured under pressure combined with magnetic fields in Ref. [26].
- [41] S. M. Thomas, C. Stevens, F. B. Santos, S. S. Fender, E. D. Bauer, F. Ronning, J. D. Thompson, A. Huxley, and P. F. S. Rosa, *Phys. Rev. B* **104**, 224501 (2021).
- [42] K. Willa, F. Hardy, D. Aoki, D. Li, P. Wiecek, G. Lapertot, and C. Meingast, *Phys. Rev. B* **104**, 205107 (2021).
- [43] C. Meingast (private communication).
- [44] Y. Tokunaga, H. Sakai, S. Kambe, Y. Haga, Y. Tokiwa, P. Opletal, H. Fujibayashi, K. Kinjo, S. Kitagawa, K. Ishida, A. Nakamura, Y. Shimizu, Y. Homma, D. Li, F. Honda, and D. Aoki, *J. Phys. Soc. Jpn.* **91**, 023707 (2022).
- [45] S. Sundar, S. Gheidi, K. Akintola, A. M. Côté, S. R. Dunsiger, S. Ran, N. P. Butch, S. R. Saha, J. Paglione, and J. E. Sonier, *Phys. Rev. B* **100**, 140502(R) (2019).
- [46] J. Rossat-Mignod, L. Regnault, J. Jacoud, C. Vettier, P. Lejay, J. Flouquet, E. Walker, D. Jaccard, and A. Amato, *J. Magn. Magn. Mater.* **76-77**, 376 (1988).
- [47] Similar falls of two temperatures scales, T_{χ}^{\max} at the maximum of the magnetic susceptibility, and T_0 at the onset of an hidden-order phase transition, were observed in the vicinity of metamagnetism in the heavy-fermion paramagnet URu₂Si₂ [59].
- [48] S. Raymond, L. P. Regnault, S. Kambe, J. Flouquet, and P. Lejay, *J. Phys.: Condens. Matter* **10**, 2363 (1998).

- [49] J. Flouquet, Y. Haga, P. Haen, D. Braithwaite, G. Knebel, S. Raymond, and S. Kambe, *J. Magn. Magn. Mater.* **272-276**, 27 (2004).
- [50] M. Sato, Y. Koike, S. Katano, N. Metoki, H. Kadowaki, and S. Kawarazaki, *J. Phys. Soc. Jpn.* **73**, 3418 (2004).
- [51] C. Lester, S. Ramos, R. Perry, T. Croft, M. Laver, R. Bewley, T. Guidi, A. Hiess, A. Wildes, E. Forgan *et al.*, *Nat. Commun.* **12**, 5798 (2021).
- [52] D. Mills and P. Lederer, *J. Phys. Chem. Solids* **27**, 1805 (1966).
- [53] R. Jullien, M. T. Béal-Monod, and B. Coqblin, *Phys. Rev. B* **9**, 1441 (1974).
- [54] T. Moriya and T. Takimoto, *J. Phys. Soc. Jpn.* **64**, 960 (1995).
- [55] A. Rosch, *Phys. Rev. Lett.* **82**, 4280 (1999).
- [56] B. Cooper, R. Siemann, D. Yang, P. Thayamballi, and A. Benerjea, in *Handbook on the Physics and Chemistry of the Actinides*, edited by A. J. Freeman and G. H. Lander, Vol. 2 (North-Holland, Amsterdam, 1985), Chap. 6, p. 435.
- [57] K. Kinjo, H. Fujibayashi, G. Nakamine, S. Kitagawa, K. Ishida, Y. Tokunaga, H. Sakai, S. Kambe, A. Nakamura, Y. Shimizu, Y. Homma, D. Li, F. Honda, and D. Aoki, *Phys. Rev. B* **105**, L140502 (2022).
- [58] Y. Ōnuki, *Physics of Heavy Fermions* (World Scientific, Singapore, 2018), Chap. 3.
- [59] W. Knafo, S. Araki, G. Lapertot, D. Aoki, G. Knebel, and D. Braithwaite, *Nat. Phys.* **16**, 942 (2020).